Geochemistry Geophysics Geosystems G3

Published by AGU and the Geochemical Society

Article
Volume 14, Number 4
24 April 2013
doi:10.1002/ggge.20046
ISSN: 1525-2027

Mantle composition controls the development of an Oceanic Core Complex

S. C. Wilson, B. J. Murton, and R. N. Taylor

National Oceanography Centre, University of Southampton, Southampton, SO14 3ZH, UK (geologygirl2002@hotmail.com)

[1] The thickness and continuity of oceanic crust is variable. Slow-spreading ridge segments often contain areas of 'amagmatic' or tectonic extension, exposing areas of lower-crust and upper-mantle, and having little or no recent volcanism. These are interspersed with areas of 'normal' volcanic crust generated by 'robust' magmatic accretion. Tectonic spreading is accommodated by displacement on low-angle extensional detachment faults, forming Oceanic Core Complexes. Although 'amagmatic' extension appears to be common at slow spreading rates, little is known about the mechanisms that drive the transition from magmatic spreading. Here, we report results from a detailed study of the Mid-Atlantic Ridge (13°N–14°N) and show, paradoxically, that despite the presence of several Core Complexes, melt production remains similar along the present-day spreading axis, which erupts homogeneous 'normal' mid-ocean ridge basalt. However, melt production during formation of the older crust off-axis was derived from substantially lower degrees of melting of a heterogeneous mantle. During this magmatically restricted phase, melt production was limited by source composition. Small volumes of an enriched basalt (M1) were produced, derived from low-fraction melts of enriched compositional heterogeneities embedded in an otherwise compositionally depleted upper-mantle, which, in turn, erupted low-fraction incompatible-element-poor basalts (M2). As a consequence of low magma flux, the crust was thin and insufficient to fully accommodate seafloor spreading. Faulting of this thin crust resulted in the development of detachment faults and the formation of OCCs. Thus, we propose that periods of low melt production, resulting directly from depleted, heterogeneous mantle drives the transition from magmatic to amagmatic spreading.

Components: 9,200 words, 12 figures.

Keywords: Oceanic Core Complex; mid-ocean ridge; slow spreading; megamullion; geochemistry.

Index Terms: 1065 Geochemistry: Major and trace element geochemistry; 1021 Geochemistry: Composition of the oceanic crust; 1032 Geochemistry: Mid-oceanic ridge processes (3614, 8416).

Received 30 August 2012; **Revised** 12 December 2012; **Accepted** 16 December 2012; **Published** 24 April 2013.

Wilson S. C., B. J. Murton, and R. N. Taylor (2013), Mantle composition controls the development of an Oceanic Core Complex, *Geochem. Geophys. Geosyst.*, *14*, 979–995, doi:10.1002/ggge.20046.

1. Introduction

[2] The past 15 years has seen a dramatic change in our view of the formation of slow spreading oceanic crust. Topographic, lithological and geophysical data from a number of slow-spreading centers have shown that plate-divergence is often accommodated by large displacement extensional detachment faulting [e.g., *Dick et al.*, 1981; *Cann et al.*, 1997; *Smith et al.*, 2006, 2008; *Tucholke et al.*, 2008; *Escartín*

et al., 2008; *MacLeod et al*., 2009]. This results in exhumation of a low-angle, domed, foot-wall massif comprising lower crust and upper mantle peridotite [e.g., *Tucholke et al*., 1998; *Ohara et al*., 2001; *Blackman et al*., 2002; *Dick et al*., 2008] collectively known as an Oceanic Core Complex (OCC). Previously, OCCs were known to occur in magma-poor areas such as ridge segment-ends, adjacent to ridge-transform intersections [*Dick et al*., 1981], and far from the locus of 3D mantle upwelling [e.g., *Tucholke et al*., 1998; *Escartín et al*., 2003]. Recent evidence, however, shows OCCs are also common at segment centers where they paradoxically indicate low magma supply or 'amagmatic' spreading [*Dick et al*., 2008; *Escartín et al*., 2008]. Here, where the proportion of magmatic spreading (M) is less than tectonic spreading (T), marks a dramatically change in normal slow-spreading mid-ocean ridge processes [*Buck et al*., 2005; *Tucholke et al*., 2008]: plate separation and crustal extension become increasingly asymmetric with the majority of strain being accommodated on large detachment faults developed on one ridge flank, while more 'normal' rift valley wall faults and abyssal hills remain on the conjugate flank [e.g., *Escartín et al*., 2008]. This asymmetry of spreading and localized high-strain leads to the exhumation of the lower crust and upper mantle, resulting in OCC formation and extensive deformation of the ridge flank.

[3] Despite a growing understanding of how OCCs develop, questions remain about what initiates them. In response to numerical models that show a strong link between melt supply and OCC formation [*Buck et al*., 2005; *Tucholke et al*., 2008], several hypotheses have begun to emerge:

(1) Local decreases in mantle temperature beneath OCC areas lead to significantly lower degrees of melting compared with magmatic sites. This would require very small-scale (15–30 km) temperature changes in the mantle.
(2) Anomalies in the thermal and/or mechanical structure of the crust at OCC areas restrict melt from reaching the surface, causing magma to be trapped at depth within the crust as dykes or gabbro bodies.
(3) Small-scale (15–30 km) variations in three-dimensional mantle upwelling results in greater melt production beneath magmatic areas compared with OCCs.
(4) Variations in mantle source composition (e.g., source depletion and/or dehydration) lead to lower degrees of melting and insufficient melt production to sustain volcanism at OCC areas.

[4] These hypotheses are all testable by examining the geochemistry of volcanic rocks erupted in association with the OCCs. Basalt geochemistry allows us to investigate the underlying mantle composition and temperature and estimate variations in its extent of partial melting and the resulting magma supply. For this purpose, we have selected a classic portion of the Mid-Atlantic Ridge, (MAR — between 13°N and 15°20′N) where a number of OCCs occur (Figure 1). In particular, we investigate the formation of a segment-centred OCC (at 13°19′N) and its relationship to mantle composition, melting and magma supply.

2. Geology of the 13°N–15°20′N Segment (MAR)

[5] The 13°19′N OCC is one of four OCCs identified on the MAR between 13°N and 15°20′N [*Smith et al*., 2006]; the other three being centred on 13°48′N, 13°30′N and 13°02′N. These volcanically starved areas of the ridge segment are separated along-strike by 10- to 20-km-long sections with robust magmatic spreading axes. Differences in their morphology, volcanic, and tectonic state have been interpreted as representing different stages in a life cycle of OCC evolution [*MacLeod et al*., 2009].

[6] The OCC at 13°19′N MAR extends for ~11 km along the strike of the spreading axis and is considered to be in an actively forming stage with continued tectonic extension along a broad, domed, and shallow detachment fault overlying a foot-wall core of serpentinized peridotite (Figure 2) [*MacLeod et al*., 2009]. In this area, we sampled basaltic material both along and across the strike: from a position just beyond the OCC breakaway (the oldest part of the detachment fault), across the youngest parts of the spreading axis, and back into older crust forming the conjugate wall of the axial valley (Figure 3). These samples provide an eruptive time series, from initiation to (near) termination of the OCC, and fall naturally into three tectonic groups:

1. Breakaway lavas — a cohesive unit erupted axial and subsequently moved off axis by slip on the detachment fault.
2. Axial lavas — in situ on the current magmatic axis.
3. Basaltic talus — hanging wall debris originally erupted at the spreading axis and subsequently eroded and stranded on the OCC dome as it developed.
4. Analytical Techniques.

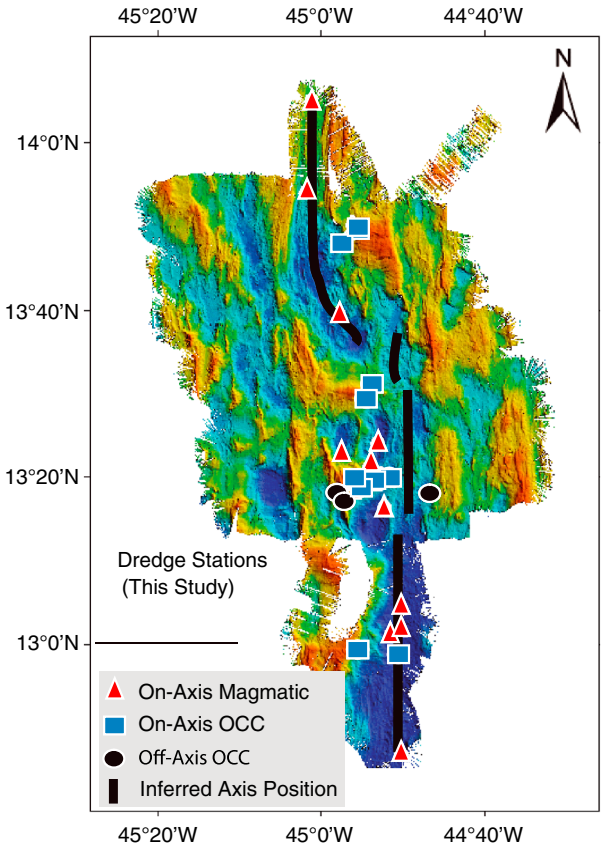

Figure 1. ArcGIS processed Simrad EM-120 bathymetry map showing the 30 stations dredged along the MAR (12°60′N–14°N), during Cruise JC007 of the RRS James Cook (2007). Also sampled are the 13°19′N OCC and adjacent magmatically-spreading neovolcanic terrains. Red triangles — axial magmatic sites, blue squares — axial OCC sites, black circles — off-axis samples. Black line denotes inferred position of the current axis. For full detail of dredge locations, see supplementary data.

[7] Whole rock major element analyses were performed by WD-XRF (Phillips Magix Pro). Trace element data were analyzed by solution ICP-MS (Thermo X-Series). Volatile data for basaltic glass were collected using FTIR (Nicolet FTIR Bench). Pb, Nd, and Sr isotope ratios were analyzed by TIMS (VG Sector 54), Pb was analyzed using a double-spike method. For standard reproducibility, precision, and accuracy data, see supplementary material.

4. Results

4.1. Axial Lava Geochemistry, 13°N–14°N

[8] Major, trace-element and isotopic data for basaltic lavas erupted between 13°N and 14°N along the present-day MAR spreading-axis show a range of compositions. Mildly alkali, trace-element, and light rare earth element (LREE) enriched mid-ocean ridge basalts [known as E-MORB — *Hofmann*, 1988] are found in the vicinity of the '14°N MAR enrichment anomaly' [*Hémond et al.*, 2006], while increasingly depleted, more normal mid-ocean ridge basalts (N-MORB) are found progressively southward toward the Marathon fracture zone at 13°N [*Donnelly et al.*, 2004; *Hémond et al.*, 2006 — Figure 4]. The E-MORBs are enriched in elements that are incompatible during peridotite melting (e.g., Sr, Nb, Nd, Ce, Zr, U, Pb, Ta and La), however, they also have lower concentrations of similarly incompatible elements: Y and Yb. Some lavas have larger amounts of incompatible element enrichment that extend the lava compositions into the ocean island basalt (OIB) field. Although *Escartín et al.* [2008] argued that similar geochemical variations could be used to distinguish between areas of asymmetric (amagmatic)

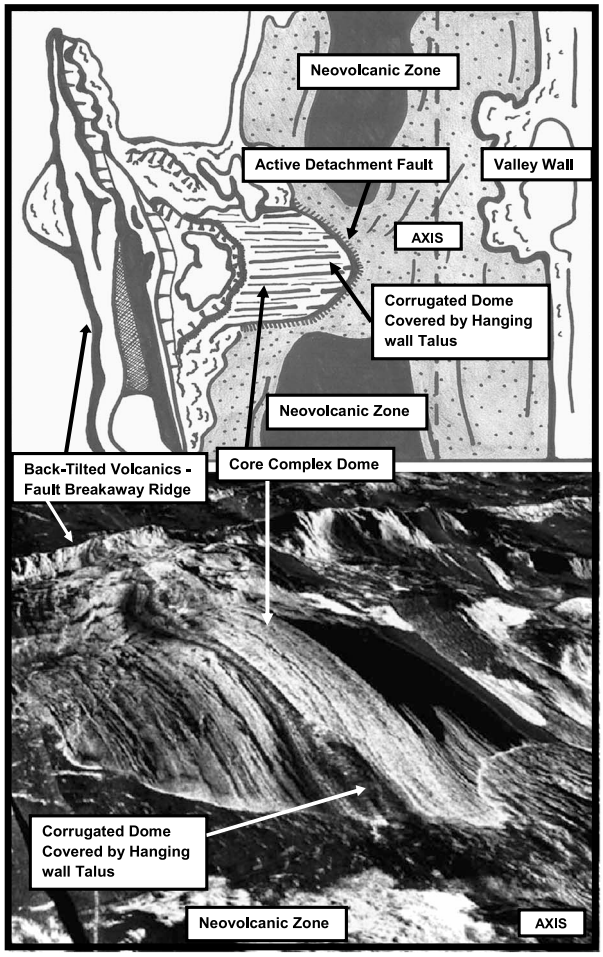

Figure 2. Top: sketch map — morphological characteristics of the 13°19′N OCC. Bottom: TOBI/bathymetry]image of the OCC generated by Fledermaus®. TOBI image modified from *MacLeod et al.* [2009].

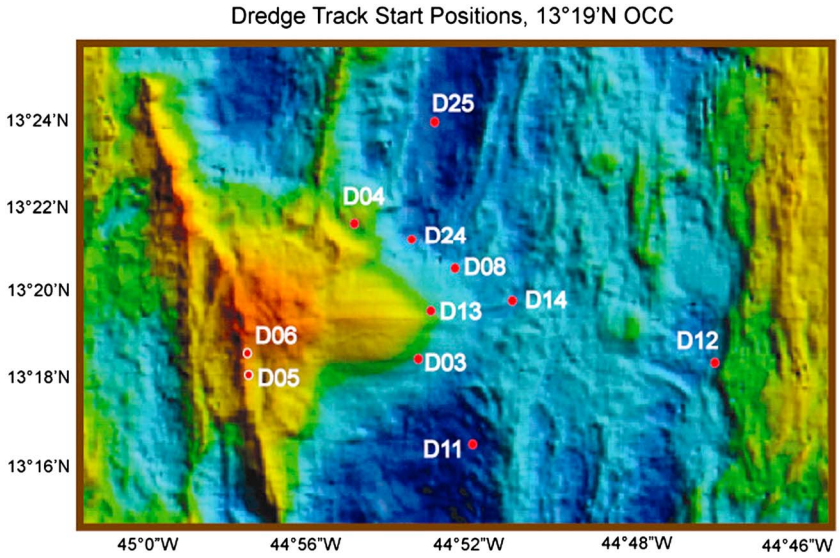

Figure 3. ArcGIS processed Simrad EM-120 bathymetry map showing the stations dredged on and around the 13°19′'N OCC. Red dots show dredge track start points. For full detail of dredge locations, see supplementary data.

and normal magmatic spreading along the MAR, these differences in present-day axial basaltic lava composition are not reproduced here (Figure 5), and we find no systematic differences in composition of axial lavas either opposite to or in between the OCCs.

4.2. Pre-OCC Lavas

[9] Lavas currently located at the OCC breakaway ridge, and its conjugate on the eastern valley wall (13°19′N), were erupted on the spreading axis at some time prior to OCC initiation and subsequently moved ~9 km to their present-day off-axis position by seafloor spreading. Using the asymmetric plate separation rates given by *MacLeod et al.* [2009] and a palinspastic reconstruction across the spreading ridge, we calculate that these lavas were erupted ~0.5–1 Ma prior to the initiation of the OCC detachment fault.

[10] Two groups of pre-OCC basalts have been identified: 'M1' (LREE enriched E-MORB) and 'M2' (LREE depleted N-MORB like lavas). Both groups are compositionally distinct from the present-day axial lavas and commonly contain clinopyroxene. In terms of their major element compositions, M2 lavas share similarities with the axial basalts, whereas M1 lavas have significantly higher concentrations of Na_2O, K_2O, P_2O_5, TiO_2, and lower CaO (Figure 5). They are also enriched in incompatible trace-elements Sr, Nb, Nd, Ce, Zr, U, Pb, Ta, and La (Figure 6) and have LREE-enriched profiles with some heavy rare earth element (HREE) depletion (e.g., low Dy/Yb

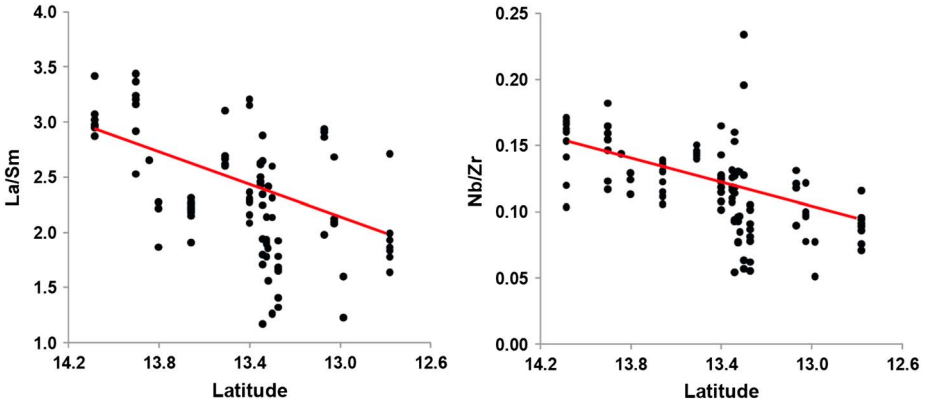

Figure 4. Basalt major element data versus latitude along the MAR (12°60′N-14°N). Red triangles — axial magmatic sites, blue squares — axial OCC sites, black circles — off-axis samples. Whole rock major element analyses were performed by WD-XRF (Phillips Magix Pro). For standard reproducibility, precision and accuracy see supplementary data.

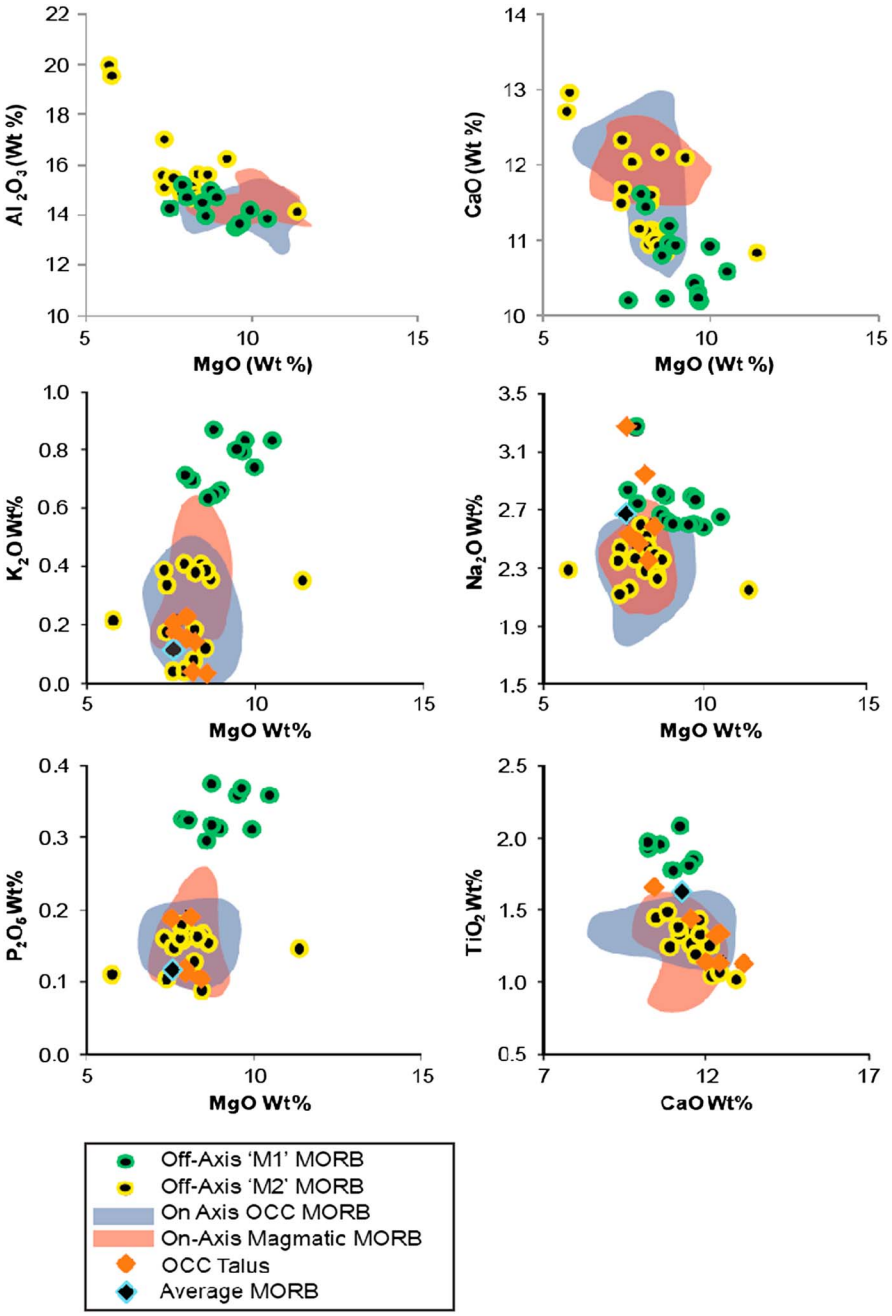

Figure 5. Major element concentrations of axial magmatic (red field) and axial OCC basalt (blue field), overlain with off-axis OCC data (M1 — green/black, M2 —— yellow/black). Blue/black diamond shows average MORB data [*Hofmann*, 1988]. For Na, P, K and Ti, orange diamonds show the composition of dolerite dyke samples from the OCC toe at 13°19'N. Error bars lie beneath display markers. *Escartín et al*. [2008] used geochemical variation in basaltic glass from the central MAR to distinguish between areas of asymmetric (amagmatic) and normal magmatic spreading, with asymmetrically spreading sites having more primitive compositions, with higher Na_2O and lower CaO than symmetrical sites. These differences are not reproduced here by the present-day axial basalts. Red triangles — axial magmatic sites, blue squares — axial OCC sites.

— Figure 7). These features indicate the M1 lavas are derived from small degrees of mantle melting, and the depressed Dy/Yb indicates some melting occurred within the garnet stability field (i.e., depths >60 km, e.g. *Yoder and Tilley* [1962]). Positive Eu anomalies (and high Al_2O_3 vs. Mg#), indicative of plagioclase accumulation, are absent in the M1 group. They are, however, common in M2 lavas and ubiquitous in the axial basalts. Significantly, some relatively unaltered dolerite dykes that were emplaced vertically into

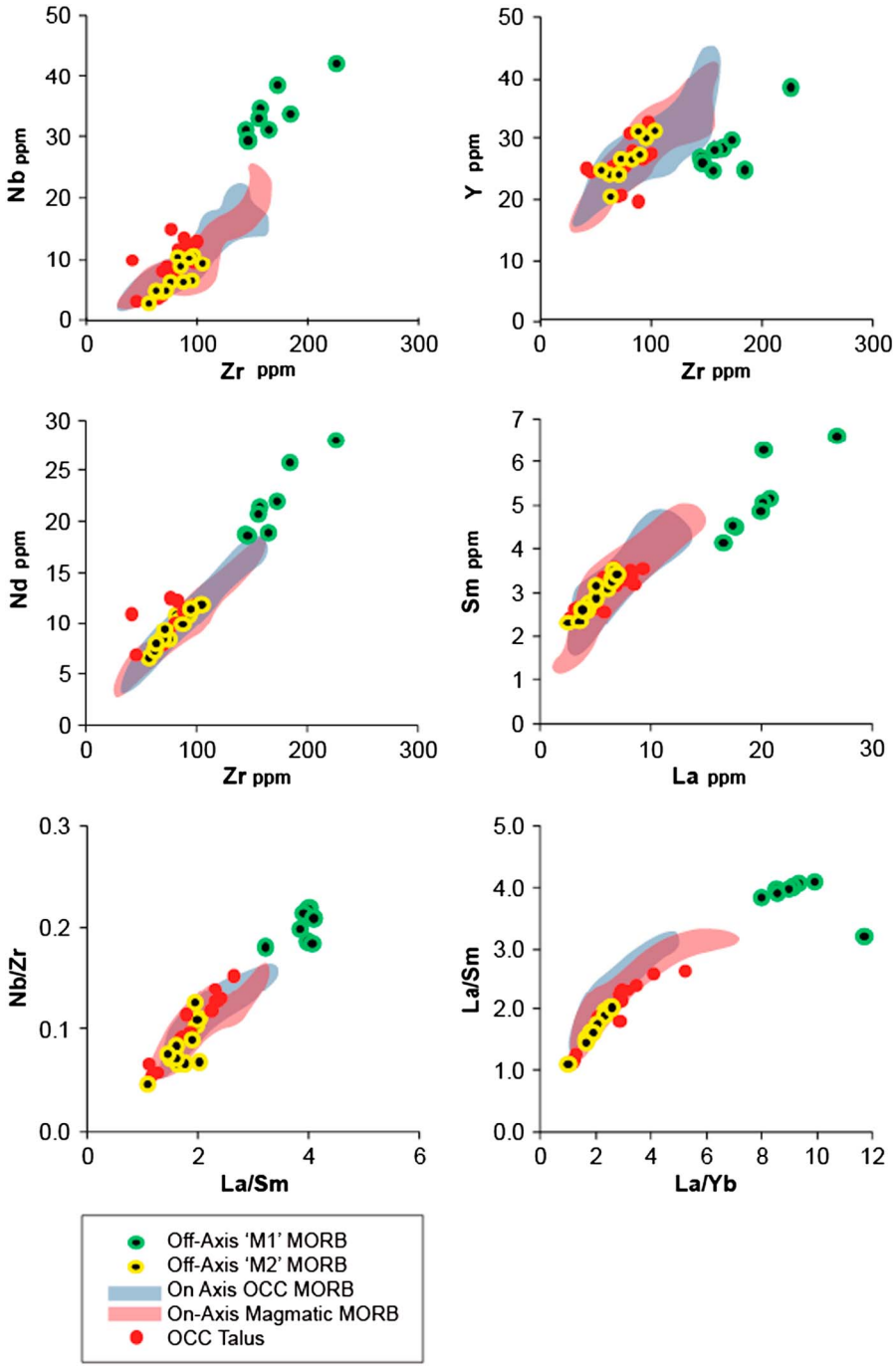

Figure 6. Trace element/ratio plots illustrate bimodality of M1 (green/black) and M2 (yellow/black) basalt compositional groups (13°19′N). Basaltic talus from the OCC (orange) is geochemically similar to M2. Axial data (13°N–14°N) (magmatic — red, OCC — blue) also shown. Error bars lie beneath display markers. Trace element data were analyzed by solution ICP-MS (Thermo X-Series). For standard reproducibility, precision and accuracy, see supplementary data.

the tilted and back-rotated mantle peridotite host-rock forming the core of the OCC 13°19′N OCC footwall dome, have major element geochemistry comparable to the present-day axial basalts at the same latitude. The vertical orientation and lack of high-grade metamorphism of these dykes indicates they are late-stage intrusive bodies emplaced after the footwall had been uplifted and partially exhumed.

4.3. Isotopic Trends

[11] M1 and M2 lavas also differ significantly from the present-day axial basalts in terms of their Pb,

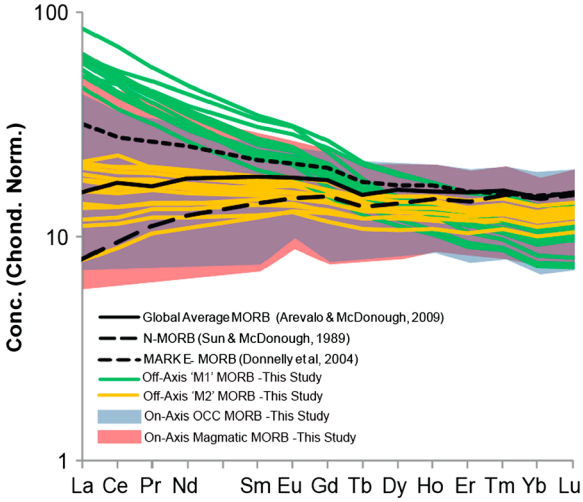

Figure 7. REE plots show axial magmatic (red field) and axial OCC (blue field) basalts (13°N-14°N). Off-axis M1 (green) and M2 (yellow) basalt groups from the 13°19'N OCC also shown. Typical N-MORB [*Sun and McDonough*, 1989], Global Average MORB [*Arevalo and McDonough*, 2009] and MARK E-MORB [*Donnelly et al*., 2004] compositions for comparison.

Nd and Sr isotope ratios (Figure 8, Table 1). M1 basalts have high $^{206}Pb/^{204}Pb$ and $^{87}Sr/^{86}Sr$, low $^{143}Nd/^{144}$ Nd, more radiogenic $^{206}Pb/^{204}Pb$ ratios than the local axial lavas and, as a result, lie on a trend extending off the local isotopic array. The parameters $\Delta^{207}Pb/^{204}Pb$ and $\Delta^{208}Pb/^{204}Pb$ describe the distance of a sample from a point on the northern hemisphere reference line (NHRL) with the same $^{206}Pb/^{204}Pb$ (the distance being expressed in units of $^{207}Pb/^{204}Pb$ and $^{208}Pb/^{204}Pb$ respectively [*Hart*, 1984]). M1 lavas have exceptionally low $\Delta^{208}Pb/^{204}Pb$, extending down to less than −40, and projecting well outside the North Atlantic MORB array. M2 lavas lie at the less radiogenic-end of the local Pb isotope compositions, but are not atypical for North Atlantic MORB as a whole (e.g., comparative data from PetDB). They also have low $^{87}Sr/^{86}Sr$ and high $^{143}Nd/^{144}Nd$, in keeping with a time-integrated, incompatible trace-element depleted composition (e.g., including low Rb/Sr and Sm/Nd ratios).

[12] Talus, found scattered across the 13°19′N OCC serpentinized peridotite dome, is thought to originate as tectonically eroded fragments of basaltic lava, dragged off from either the OCC breakaway ridge, the hanging wall at the OCC detachment fault termination, or both. These fragments of lava do not show the same range of chemical variation seen in the *in situ* off-axis lavas (from the breakaway and its conjugate). Nor do they completely resemble the adjacent axial volcanics (Figure 6). Instead, they appear to represent fragments of lavas erupted during a transition in volcanism from the M2 small melt fraction lavas to the more 'normal' axial lavas.

5. Discussion

[13] The MAR between 13°N and 15°20′N is both morphologically and geochemically unusual. *MacLeod et al*. [2009] show that where there is a reduction in recent volcanic activity at the spreading axis, the adjacent off-axis magmatic crust is tectonically thinned and, in places, removed by large displacement detachment faulting and the formation of OCCs. The OCCs here are analogous to those commonly found at ridge segment-ends where the lithosphere is thought to be thick, cold and magma-starved. However, models for 3D mantle upwelling at slow spreading ridges, like the MAR at 45°N, predict that the segment centers should be magmatically well supplied and have thick crust and well-established volcanic spreading (*Lin et al*. [1990]).

[14] Various models have been developed to describe OCC development, usually involving a reduction in the contribution of magmatic spreading (M). However, there are few theories explaining OCC initiation mechanisms. For example, *Escartín et al*. [2008] use MgO vs. Na_2O, CaO and FeO concentrations in basaltic glass (MAR) to distinguish between areas of amagmatic (asymmetric) and normal magmatic (symmetric) spreading. Although basalts from the present-day axial sites opposite OCCs, between 13°N and 14°N MAR, have slightly higher Na and Fe concentrations than their magmatic spreading axial counterparts, the low CaO trend reported by *Escartín et al*. [2008] is not found here. Nor is there any significant compositional (incompatible trace-element) evidence for systematically reduced melt fraction, or isotopic evidence for systematically different mantle sources, beneath the present-day ridge axis at sites located opposite the OCCs when compared with neighbouring magmatically robust spreading sites. Thus, contrary to *Escartín et al*. [2008], there is no convincing correlation between current spreading style and present-day basalt geochemistry in this section of the MAR.

[15] However, this was not the case 0.5 to 1 Ma ago; at the time the magmatic crust that was later tectonically dissected and extended by OCC formation was being formed. Here, at 13°19′N, off-axis basalts record magmatic conditions at the spreading ridge-axis

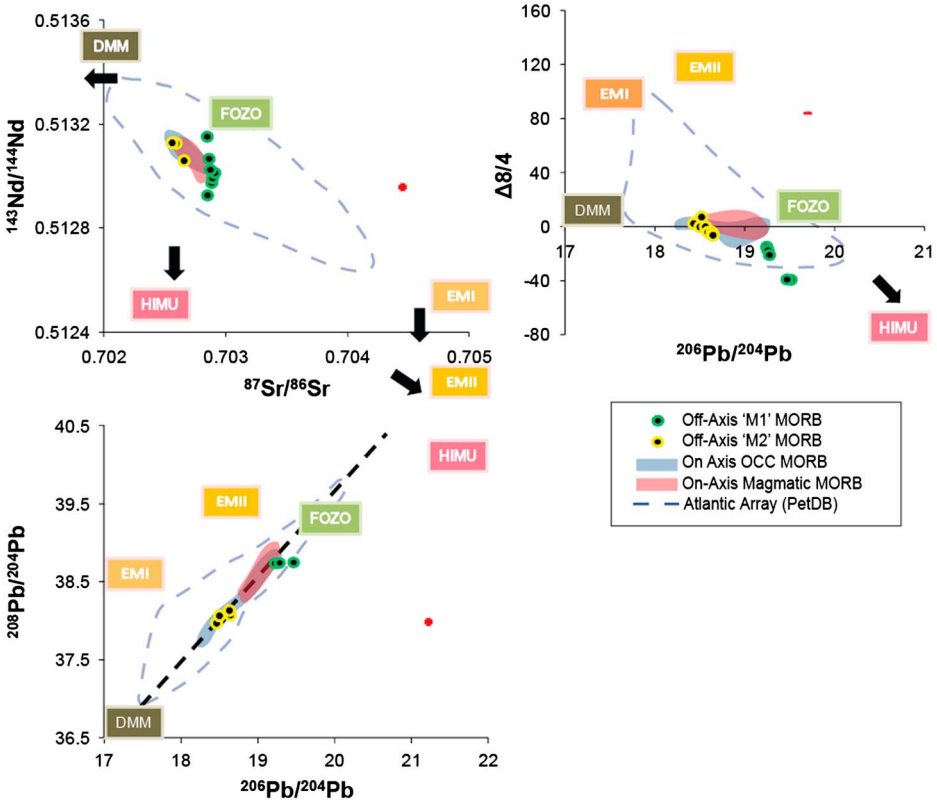

Figure 8. $^{208}Pb/^{204}Pb$ vs. $^{206}Pb/^{204}Pb$, $^{143}Nd/^{144}Nd$ vs. $^{87}Sr/^{86}Sr$ and $\Delta^{208}Pb/^{204}Pb$ vs. $^{206}Pb/^{204}Pb$ isotope data for the Atlantic (PetDB), 12°60 N'-14°N axial (magmatic — red, OCC — blue), M1 (green/black) and M2 (yellow/black) off-axis basalts (13°19'N). Data considered in terms of mantle source end-member components DMM, EMI, EMII, HIMU and FOZO. Error bars shown in red. The parameters $\Delta^{207}Pb/^{204}Pb$ and $\Delta^{208}Pb/^{204}Pb$ represent the distance of a sample from a point on the NHRL with the same $^{206}Pb/^{204}Pb$, the distance being in units of $^{207}Pb/^{204}Pb$ and $^{208}Pb/^{204}Pb$ respectively [*Hart*, 1984]. Error bars lie beneath display markers. Pb, Nd and Sr isotope ratios were analyzed by TIMS (VG Sector 54). For analysis details and standard reproducibility see supplementary data.

just prior to OCC initiation. The bimodal compositions of these lavas (M1 and M2) differ from the adjacent axial lavas in terms of their major and trace element compositions and isotope ratios. This suggests that they experienced different extents and depths of melting and melting path lengths, and/or local variations in source mantle composition.

[16] Major and trace-element data for the off-axis M1and M2 lava groups indicate differences that are not the result of basaltic crystallisation, e.g., some of the most incompatible trace-element enriched lavas are also the most primitive (highest Mg#). Instead, differences within the off-axis lavas indicate different extents and depths of mantle melting, or localised variations in mantle source composition. For example, compared with M2 basalts, the higher Zr/Y for M1 basalts may indicate lower melt fraction while the higher La/Sm and Nb/Zr indicate greater mantle source enrichment [*Hofmann*, 1988].

[17] Lower Yb/Lu and higher Dy/Yb ratios also suggest residual garnet in the M1 mantle source and hence initial depths of mantle melting (exceeding ~60 km) [*Hellebrand et al.*, 2002]. Such a situation is analogous to the 'cold, thick lithospheric lid effect' invoked for the Romanch Transform Fault to ridge intersection [*Bonnati et al.*, 2001], where lateral thermal conduction cooled and thickened the lithosphere suppressing shallow mantle melting. As a result, the thicker lithosphere causes deeper cessation of melting and thus the primary magmas are compositionally weighted toward a higher proportion of melt-fractions derived from the bottom of the mantle melting column. In contrast to the M1 lavas, the M2 basalts do not show a strong garnet effect, indicating that the primary magmas are compositionally weighted toward shallower melt fractions and little, if any, melting took place in the garnet stability field (Table 1). Such magmas would result if the lithosphere was thinner and hence less cold such that mantle melting could continue to shallow asthenospheric depths.

[18] While the common presence of primitive (high-Mg) clinopyroxene in the OCC basalts might

Table 1. Average Major, Trace Element, and Isotopic Basalt Compositions for the 13–14°N Area of the MAR.

	M1	M2	Axial		M1	M2	Axial
SiO_2 (wt%)	48.79	49.71	49.50	Sm	4.97	3.10	3.13
TiO_2	1.81	1.40	1.26	Eu	1.70	1.11	1.14
Al_2O_3	14.84	15.22	15.47	Gd	5.24	3.91	3.83
Fe_2O_3	10.29	10.25	10.45	Tb	0.82	0.69	0.67
MnO	0.16	0.17	0.17	Dy	4.79	4.44	4.26
MgO	8.60	8.32	8.06	Ho	0.92	0.94	0.90
CaO	11.04	11.29	11.44	Er	2.48	2.68	2.55
K_2O	0.67	0.37	0.32	Tm	0.34	0.40	0.38
Na_2O	2.65	2.37	2.34	Yb	2.13	2.57	2.45
P_2O_5	0.32	0.18	0.16	Lu	0.31	0.38	0.37
SO_3	0.14	0.15	0.19	Hf	3.60	2.14	2.24
Li (ppm)	4.90	5.19	5.11	Ta	1.88	0.53	0.61
Sc	29.13	30.95	38.70	Pb	1.57	0.79	0.87
Rb	13.01	4.20	6.11	Th	1.75	0.32	0.69
Sr	353.84	140.03	188.02	U	0.62	0.19	0.25
Y	26.32	25.87	25.65	H_2O	0.60	0.27	0.38
Zr	167.20	86.17	92.30	$^{206}Pb/^{204}Pb$	19.32	18.55	18.82
Nb	32.53	7.98	11.21	$^{207}Pb/^{204}Pb$	15.60	15.51	15.54
Cs	0.18	0.08	0.08	$^{208}Pb/^{204}Pb$	38.73	38.05	38.36
Ba	192.46	49.67	76.37	d7-4	1.95	0.66	0.59
La	19.18	5.81	7.56	d8-4	−25.27	−0.14	−2.41
Ce	40.13	14.33	17.34	$^{143}Nd/^{144}Nd$	0.51	0.51	0.51
Pr	4.97	2.13	2.42	$^{87}Sr/^{86}Sr$	0.70	0.70	0.70
Nd	20.93	10.23	11.11				

All data from this study. Major elements expressed in wt %, trace elements in ppm.

indicate deep onset of crystallization (at pressures ~10 kbar), which would in turn be consistent with a cold and thick lithosphere, alternatively primitive clinopyroxene also may develop at relatively shallow depths when the source mantle is highly depleted (high CaO/Al_2O_3) and as a result of melt/olivine reaction [*Suhr et al.*, 1998; *Lissenberg and Dick*, 2008; *Drouin et al.*, 2009]. The latter is more consistent with the 13°–14°N MAR mantle peridotite which is known to be anomalously depleted [*Dosso et al.*, 1993; *Seyler et al.*, 2007; *Godard et al.*, 2008; *Suhr et al.*, 2008] and which shows abundant evidence for melt-rock interaction [*Seyler et al.*, 2007; *Pertsev et al.*, 2009].

[19] Alternatively, a highly depleted (low Al_2O_3) source mantle with some variable enrichment would be able to produce the variety of 'garnet effects' described above for M1 and M2 melts, without the requirement for variable melt path length or depth of onset. Isotope data (Figure 8) suggest that basalts from 13°N to 14°N form by a combination of both depleted MORB mantle (DMM) with enriched high μ (HIMU) + Focus Zone (FOZO) sources. HIMU sources are enriched in U and Th relative to Pb, without an accompanying increase in Rb/Sr. M1 basalts have high U/Pb and Th/Pb values, but Rb/Sr ratios lie within the present-day axial basalt array. M1 basalts have trace-element compositions that are similar in enrichment to HIMU OIB material, but do not resemble enrichment arising from other enriched mantle sources (e.g., EMI or EMII — see *Armienti and Gasperini* [2007]).

[20] While isotope compositions for both axial and M2 lavas form arrays between DMM, HIMU, and FOZO mantle components, M1 basalts lie on a single trend extending toward HIMU from a point between DMM and FOZO. This indicates that source (or melt) mixing, dominated by the most enriched end-members, generated the M1 lava series. In this sense, HIMU also appears to contribute more to the formation of M2 basalts than to the axial array, as is particularly evident within the $\Delta^{208}Pb/^{204}Pb$ vs. $^{206}Pb/^{204}Pb$ plot (Figure 8).

[21] Isotope vs. trace-element ratio data (Figure 9) show that M1 basalts are characterised by having the most time-integrated enrichment (i.e., having radiogenic Sr and Pb, and unradiogenic Nd) in terms of their mantle source, and M2 basalts have some of the most time-integrated depleted compositions. Good correlations between isotopic ratios and incompatible trace elements indicate that the M2 compositional array results primarily from variations in ancient, time-integrated, source enrichment rather than more recent melting events. Similar relationships apply to M1 basalts, but these lavas

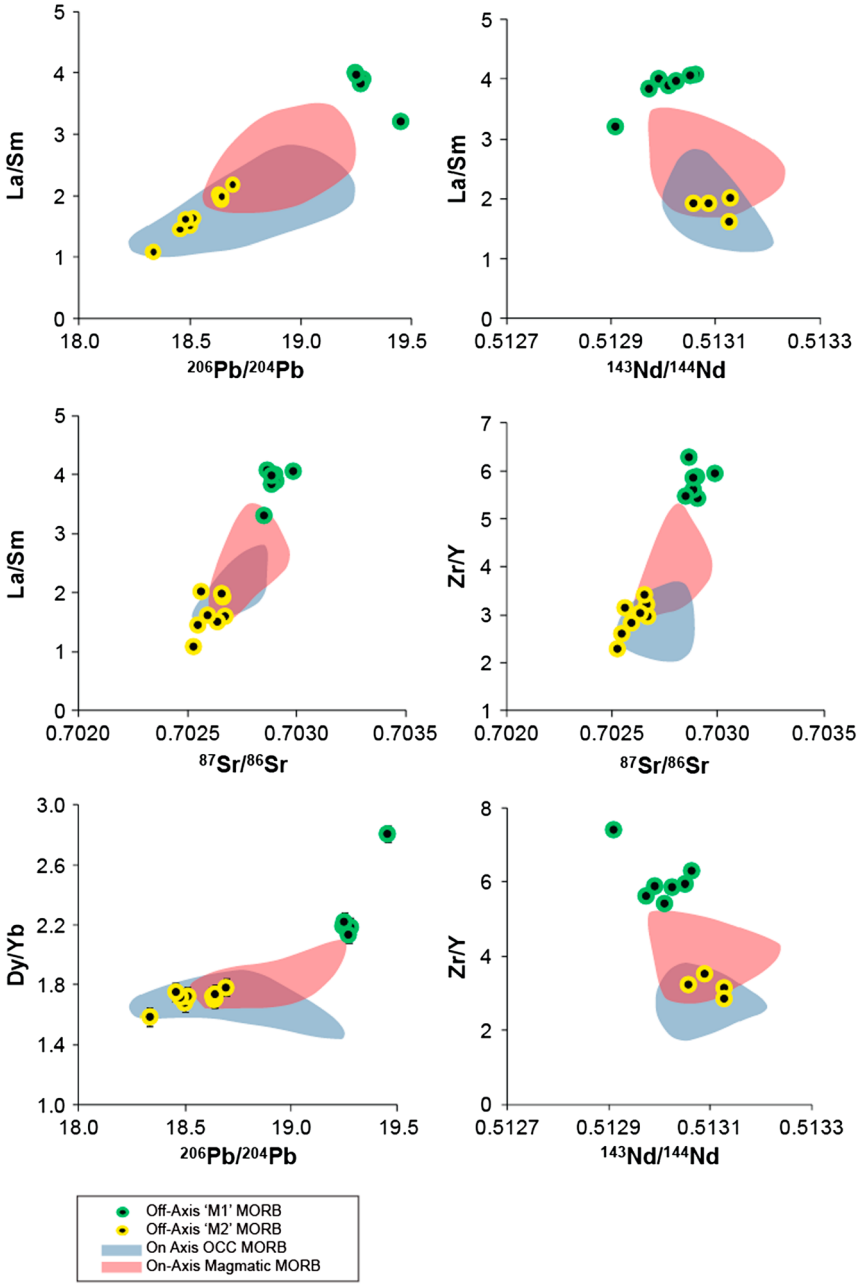

Figure 9. $^{206}Pb/^{204}Pb$, $^{87}Sr/^{86}Sr$ and $^{143}Nd/^{144}Nd$ isotope vs. trace element ratio plots to distinguish source enrichment from melt fraction effects in axial (magmatic — red, Axial OCC — blue, 13°N-14°N) and off-axis M1 (green/black) and M2 (yellow/black) basalts. Error bars lie beneath display markers.

form compositional arrays that are discordant to both axial and M2 lavas, suggesting significant contributions from different enriched end-member sources, and a reduced contribution from UDMM relative to the M2 lavas. This supports the findings from the isotope data that the formation of M1 magmas can be attributed to mixing primarily between HIMU and FOZO.

[22] Basaltic talus from the dome of the 13°19′N OCC, which was erupted at the magmatic axis and subsequently broken up and deposited on the detachment surface, has trace element compositions similar to the M2 basalts. However, it is compositionally distinct from the M1 lavas supporting the notion that, based on our isotopic data, M1 melts were produced for only a brief period in time prior to the initiation of the OCC.

[23] The extreme compositional bimodality of the 13°19′N OCC lavas provides an insight into their eruption sequence. Broad compositional ranges in

MORB are commonly produced where small amounts of coexisting melt are infrequently tapped and mixed. However, the distinct bimodality between M1 and M2 lavas further suggests that these different melt batches remained isolated from each other as they percolated through the upper-mantle and crust. Both the diversity of melt compositions and their relatively unmixed character are compatible with low extents of melt production from a heterogeneous mantle source. We suggest that, initially, M1 melts were formed when a region of mantle beneath the ridge axis containing small heterogeneities (veins) of more fusible HIMU-FOZO material (eclogite and/or pyroxenite) was melted. As a result, the mantle was cooled by both advective heat loss, as the melts migrated upwards, and by latent heat of fusion resulting in a hiatus of melting. Following this hiatus, as mantle upwelling progressed, small-fraction melting of the now cooler and ultra depleted MORB mantle (i.e., UDMM) produced M2 type magmas. This processes generated the bimodal chemistry, geographical distribution and temporal evolution of the 13°19′N OCC basalt types seen today.

5. Geochemical Modeling

[24] To test the idea that M1 and M2 magmas were derived from different melt fractions and mantle compositions, we use simple a fractional melting model [*Shaw*, 1970; *McKenzie and O'Nions*, 1991]. The model assumes a range of homogeneous mantle sources formed by different combinations of HIMU [*Hannigan et al*., 2001] and UDMM [*Workman and Hart*, 2004]. For simplicity, the model adapts a single set of mineral modes for all combinations of DMM-HIMU, but varies the proportion of garnet in the source (regardless of whether this arises from deep melting within the garnet field, or by shallower melting of enriched veins carrying a ghost garnet signature into a low-Al_2O_3 harzburgitic host). Here, we find that a HIMU-enriched UDMM source composition reproduces our melts better than average/depleted UDMM variants. This enriched melt composition is generated assuming closed-system melting of a homogeneous mantle source, whereby energy or heat can be transferred to or from the surroundings, but no melt can leave the system. This results in early saturation in Mg-rich clinopyroxene in melts that closely matching our observed, primitive clinopyroxene-bearing basalts. The addition of a clinopyroxene-rich component (not normally present in DMM) is consistent with metasomatic processes such as refertilizing of the mantle by small melts, and corroborates evidence of melt-rock interaction found in dredged peridotites from the region [*Seyler et al*., 2007; *Pertsev et al*., 2009].

[25] Inverse modelling of the lavas at 13°19′N shows that the addition to the mantle of a third (enriched) component, which increases its middle rare earth element (MREE) content, significantly improves the fit of the binary DMM-HIMU source melting model to natural M1 lava compositions (Table 2, Figure 10). In these lavas, the proportional contribution of the third component appears to be significant. The addition of this third component(s) is not 'special pleading' and compliments previous findings that predict the presence of mantle components, with lower LREE and higher M-HREE compositions than HIMU, for the central MAR *Hannigan et al*. [2001]. The results from our own models also predict a (0–5%) contribution from a low HIMU mantle component to M2 lavas, but a much higher (20–40%) contribution from a HIMU component for the M1 lavas. This is consistent with our isotopic evidence, which also suggests that M1 derive from an enriched source, with a substantially lower contribution from the more refractory UDMM source, compared with the M2 lavas or axial lavas. However, the difference may be partially due to higher melt fraction melting of M2 (4–10%): higher melt fractions from a UDMM source result in significant dilution of the HIMU component in the resulting cumulative melt composition. This is consistent with our geochemical data that predict the reduction in contribution from the HIMU component in M2 is a result of enriched material, having been previously melted from the source to form M1 lavas. In addition to identifying mantle components, our modeling also predicts a variable 'garnet effect' in the mantle sources, the amount of which is linked to the extent of partial melting. Modeled low-melt-fractions are associated with greater garnet signatures in the source, with M1 having an estimated 10–25%, and M2 between 20% and 50%.

[26] Usually, high proportions of garnet in the mantle source are compatible with fertile (Ca and Al-rich) mantle compositions, yet the mantle underlying the

Table 2. Outcomes of Mantle Source Modeling, This Study.

Melt ID	Melt Fraction	HIMU, %	Length of Melt Path
M1 Lavas	3–4%	20–50	~100–45 km
M2 Lavas	4–10%	0–5	~100–55 km
Axial	2–12%	0–5	~100–30 km

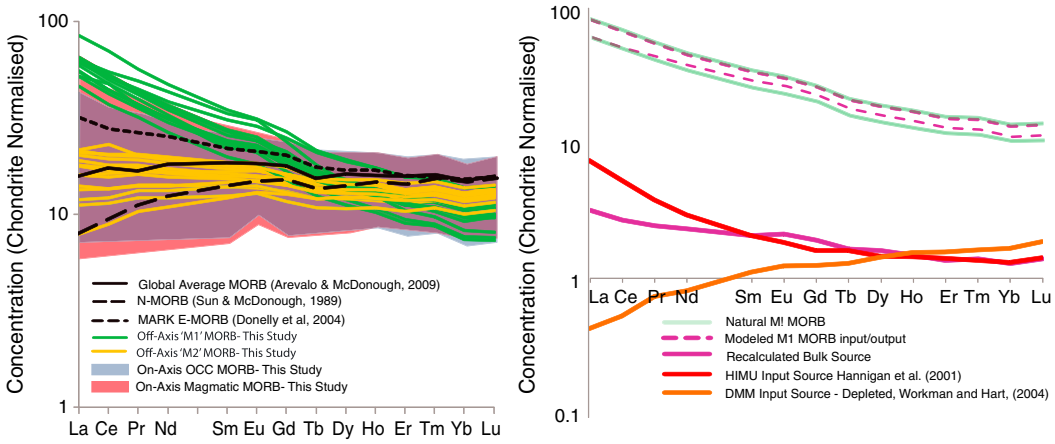

Figure 10. Outcomes of geochemical modeling. Left — variation between natural (solid) and modelled (dashed) basalt compositions (13°19'N). Also shown are HIMU [*Hannigan et al*., 2001] and UDMM compositions [*Workman and Hart*, 2004]. Right — recalculation using modified bulk source.

13°–14°N MAR is thought to be unusually refractory [*Seyler et al*., 2007; *Godard et al*., 2008; *Suhr et al*., 2008]. This suggests that the garnet effects, seen in M1 and M2 lavas, arise from preferential melting of enriched, 'garnet-like' metasomatized veins within a host of depleted (harzburgitic) mantle, yielding low-melt-fraction melts with a strong garnet signature, rather than actual melting of fertile garnet lherzolite mantle.

7. Model for OCC development —13°–14°N

[27] OCCs are distributed throughout the Mid-Atlantic Ridge between 13°N and 14°N, where they are flanked by regions of normal and robust magmatic spreading. Sonar images show that opposite the OCCs recent volcanic activity and lava flows are absent in the rift axis, supporting the concept that OCC development is a consequence of low melt supply.

[28] Despite the evidence for diminished volcanic activity, basalt geochemistry shows that there are no consistent or significant differences in melt fraction for present-day axial lavas either opposite the OCCs or in between where volcanic activity appears robust. Instead, the calculated melt fraction of ~12% remains broadly similar throughout the spreading axis. It is therefore unlikely that current variations in melt supply, possibly resulting from fine-scale mantle upwelling, either affect or cause OCC initiation and development in the 13°–14°N MAR region. In contrast, however, we show that there is a correlation between low degrees of mantle melting, resulting in the production of thin crust that was moved then off axis, and the initiation of later detachment faulting that lead to OCC development. We suggest that, for the 13°–14°N MAR section, this reduction in crustal thickness was a direct result of mantle composition resulting from an underlying mantle that was both depleted relative to an N-MORB source and later locally refertilized to generate a bimodal source prior to being melted. Normal axial-wall faulting developed in this anomalously thin crust resulted in water ingress to the shallow underlying mantle peridotite that altered to serpentinite and talc resulting in strain weakening and continued displacement on the normal fault.

[29] Near vertical dykes that cut across the domed surface of the serpentinized peridotite core of the 13°19′N OCC footwall have compositions very similar to axial lavas, suggesting that melt from the present-day spreading axis intrudes into the OCC footwall rather than being erupted. These magmas may also intrude deeper in the OCC footwall forming plutonic rocks [e.g., *Kelemen et al*., 2004]. The sparse occurrence of gabbro (~2%) at the 13°19 OCC (Table 3) suggests that this may not be such a significant mechanism here, although this may be an artefact of sampling only the surface of the study area. It is argued that the diversion of melt into the 13°19′N OCC footwall is close to terminating the detachment fault while simultaneously reducing the surface expression of volcanism opposite the OCC in the spreading axis.

8. Modeling of Small-scale Thermal Anomalies

[30] We have argued that a heterogeneous mantle composition, heat advection, and the latent heat of

fusion during early melt-extraction from enriched mantle streaks, all combined to reduce magma flux resulting in the production of thin magmatic crust that was a prerequisite to OCC formation at 13°19′N MAR. However, it is also a possible that the low melt flux at the 13°19′N OCC was a result of pre-existing cooler temperatures within the underlying mantle. To investigate this, we calculate how long a preexisting low-temperature anomaly would survive in the sub-spreading ridge mantle (Figure 11). In the absence of knowledge about the size, geometry or other characteristics of the anomaly, we only offer this estimate as a means of testing the feasibility of preserving long-term temperature anomalies in the subridge mantle asthenosphere.

[31] The geographic extent of any mantle temperature anomaly underlying 13°19′N OCC is constrained by the ~11 km width of the OCC. Using the one-dimensional heat equation $H = kA(\Delta T/x)$ [*Cannon*, 1984] where:

k = thermal conductivity
A = total × sectional area of conducting surface
ΔT = temperature difference
x = thickness of conducting surface separating the two temperatures

[32] We calculate a thermal equilibration times for a range of spherical temperature anomalies of between 2 and 98 km in diameter with temperature differentials (ΔT) of 5 to 100° K. For anomalies 10–20 km in diameter, and a temperature difference (5°K), thermal equilibration times are 30–100 ka. These times decrease substantially as ΔT increases, causing the rates of thermal equilibration to increase also. These short thermal equilibration times suggest that anomalously cooler mantle temperatures beneath OCC areas are very unlikely to be long-lived and, hence, inherited characteristics of the MAR mantle, and are therefore not the trigger for low melt fraction melting episodes. Instead, we argue that preconditioning of the UDMM mantle by major element depletion

Table 3. Rock Types and Percentage (by weight) of Rocks Sampled Per Dredge

Dredge No.	Start Lat°	Lithology (Wt %)									
		Basalt	Dolerite	Gabbro	Dunite	Harzburgite	Serpentine	Plagiogranite	Hydrothermal Minerals	Talc	Other*
1	13.82	11.1	0	5.6	0	72.2	0	0	0	5.6	5.6
2	13.49	0	35.0	5.0	25.0	0	25.0	0	5.0	0	5.0
3	13.30	0	0	0	0	0	0	0	0	50.0	50.0
4	13.36	0	0	0	0	0	100.0	0	0	0	0
5	13.30	62.5	12.5	0	0	0	6.3	0	6.3	0	12.5
6	13.30	100.0	0	0	0	0	0	0	0	0	0
7	13.30	50.0	0	0	0	50.0	0	0	0	0	0
8	13.34	50.0	0	0	0	50.0	0	0	0	0	0
9	13.32	16.7	10.0	10.0	10.0	23.3	13.3	0	0	0	16.7
10	13.34	69.2	2.6	2.6	0	0	0	0	15.4	0	10.3
11	13.27	69.7	2.7	2.6	0.1	11.7	0	0	0	0.1	13.1
12	13.30	100.0	0	0	0	0	0	0	0	0	0
13	13.32	18.2	6.8	2.3	2.3	56.8	0	0	0	2.3	11.4
14	13.33	75.0	0	0	0	25.0	0	0	0	0	0
15	13.07	94.1	0	0	0	0	0	0	0	0	5.9
16	13.03	61.1	0	0	5.6	33.3	0	0	0	0	0
17	12.98	100.0	0	0	0	0	0	0	0	0	0
18	12.96	Dredge unsuccessful									
19	12.78	100.0	0	0	0	0	0	0	0	0	0
20	12.99	19.4	30.6	16.7	5.6	2.8	13.9	0	0	0	11.1
21	13.02	0	0	0	2.4	87.8	4.9	0	0	2.4	2.4
22	13.52	Dredge unsuccessful									
23	13.51	67.4	0	7.0	0	0	0	0	16.3	2.3	7.0
24	13.35	100.0	0	0	0	0	0	0	0	0	0
25	13.40	100.0	0	0	0	0	0	0	0	0	0
26	13.66	100.0	0	0	0	0	0	0	0	0	0
27	13.80	80.0	0	0	0	0	0	0	0	0	20.0
28	13.84	9.4	7.5	3.8	11.3	39.6	1.9	13.2	0	9.4	3.8
29	13.90	100.0	0	0	0	0	0	0	0	0	0
30	14.09	100.0	0	0	0	0	0	0	0	0	0

*Other lithologies include sediments, Mn crusts, breccias, hyaloclastites, uncategorised peridotites and epidosite

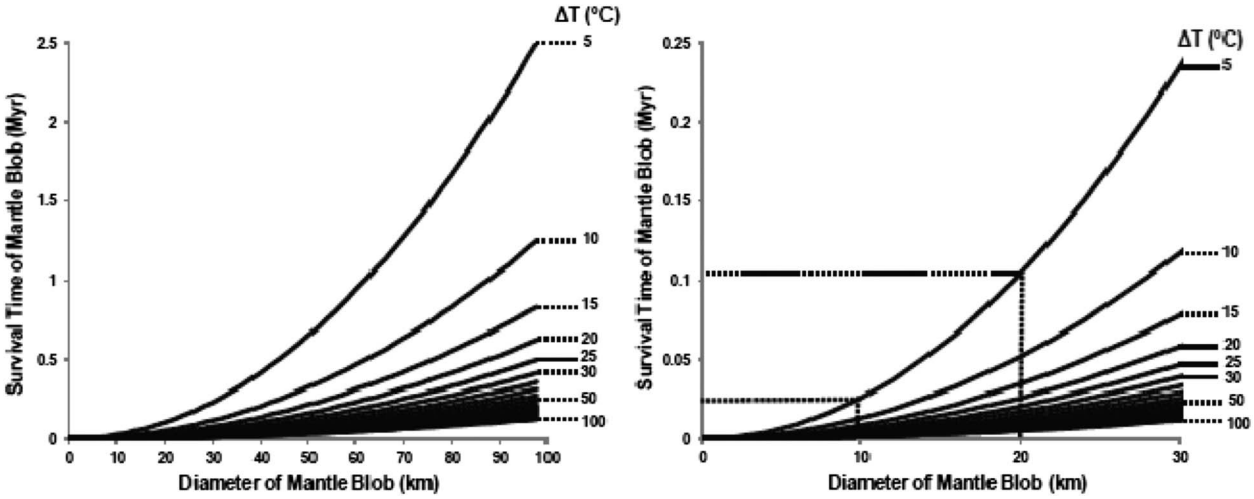

Figure 11. Plots showing results of thermal modeling. Left — survival times of modelled mantle blobs. Right — zoomed scale shows that blobs of an ideal size to contribute to OCC formation have a maximum survival time of ~100 ka.

is the main driver for low melt fraction during M1 genesis. This, coupled with the cooling effects caused by the extraction of the M2 melts, suppresses magma supply, yielding thin crust that is more susceptible to long-lived detachment faulting and OCC development.

9. OCC Initiation Driven by Mantle Heterogeneity

[33] Figure 12, stages A–E, represent mantle preconditioning, low melt production, crustal thinning and the eventual formation of long-lived detachment faulting at 13°19′N MAR that ultimately led to OCC formation.

Stage (A): magmatic spreading from a locally depleted upwelling mantle source, in which there are some enriched veins, results in low-fraction melting and a low flux of M1 melt.

Stage (B): M1-type magmas, formed from the enriched fusible veins and mixed with a little UDMM melt, generate thin magmatic crust. The resulting magmas are incompatible-element enriched and have distinct isotopic signatures, dominated by HIMU-FOZO mixing.

The removal of enriched components (during M1 genesis) promotes localized mantle cooling (by the advection of magmatic heat and the latent heat of fusion) and dehydration of the mantle source, suppressing melting of the more depleted M2 component due to the temperature gradient created by the heat of fusion of the fertile (M1) component The suppression of M2 melting, and the very low melt fraction do not allow M1 and M2 melts to homogenise, resulting in bi-modal volcanism and a compositional gap.

The occurrence of only M2-type (trending to axial type) lava compositions in talus on the OCC surface (no M1 type) may be significant, indicating that M1 and M2 magmas did not coexist for long beneath the spreading axis. We argue that after an initial melting episode stripping enriched material to form M1 melts, the enriched material was predominantly exhausted. During an episode of ongoing low-degree melting of the ascending residual mantle, only M2 type magmas continued to be formed, persisting for some time after M1 production ceased.

Stage (C): Following M1, M2 melts continued to be produced from a predominantly UDMM source, preconditioned by the earlier removal of enriched veins and cooled (by heat advection) during the formation and removal of the M1 melts. Both M1 and M2 melt production result in low magma flux and thin magmatic crust, and are precursory to the initial stages of OCC growth. The current distance from the 13°19′N OCC breakaway to the known position of the first outcrop of mantle peridotite, combined with the angle of rotation of the OCC, gives a maximum estimate of mafic crustal thickness of ~3.5 km. This is about half the thickness of average seismically measured oceanic crust at segment centers (Table 4) and supports the idea that the crust where the OCC initiated is very thin and a product of low degrees of mantle melting. Furthermore, the scarcity of gabbro (see Table 3) in our study area argues for a crustal thickness, comprising predominantly pillow basalts and sheeted dykes, of substantially less than 3.5 km.

Stage (D): With insufficient melt supply, during which magmatic axial spreading may have dramatically reduced, tectonic extension is accommodated on nearby axial valley wall normal faults that fracture the thin magmatic crust generated by M1 and M2 volcanism.

Stage (E): As a result of the shallow mantle beneath this thin crust, faulting allows easy access of seawater, causing serpentinization, localized strain weakening and continued slip on developing detachment faults. As spreading continues, these faults rotate to a shallow angle, exposing the underlying lower crust and ultramafic mantle, and resulting in OCC formation. During OCC formation, the spreading ridge begins to sample new mantle containing a higher proportion of HIMU-FOZO veins. Melt production increases in response, and magmatism at the axis becomes more evident. Triangular neovolcanic zones form and cut into the axis toward the fault line. This volcanism will eventually terminate the OCC fault, and normal magmatic spreading will resume.

10. Conclusions

[34] Here, we argue that the development of segment-centre OCC at 13°19′N MAR is a direct consequence of unusual geochemical characteristics in the underlying mantle. At segment ends and transform faults, asthenospheric heat is lost by lateral conduction into older colder lithosphere, resulting in lower melt production, thinner crust and the formation of OCCs. However, at 13°N–14°N MAR, in the center of the ridge segment and far from the influences of any transform offset, extreme mantle source depletion followed by heat loss from early melting of enriched heterogeneous veins results in a reduction of melt flux that, in turn, yields thinner magmatic oceanic crust. Faulting, serpentinization and strain weakening of this anomalous lithosphere subsequently results in continuous slip on normal axial wall faults, triggering detachment faulting and OCC formation. We show that long-lived thermal anomalies (mantle cold spots) cannot survive long enough to be the cause of suppressed melt

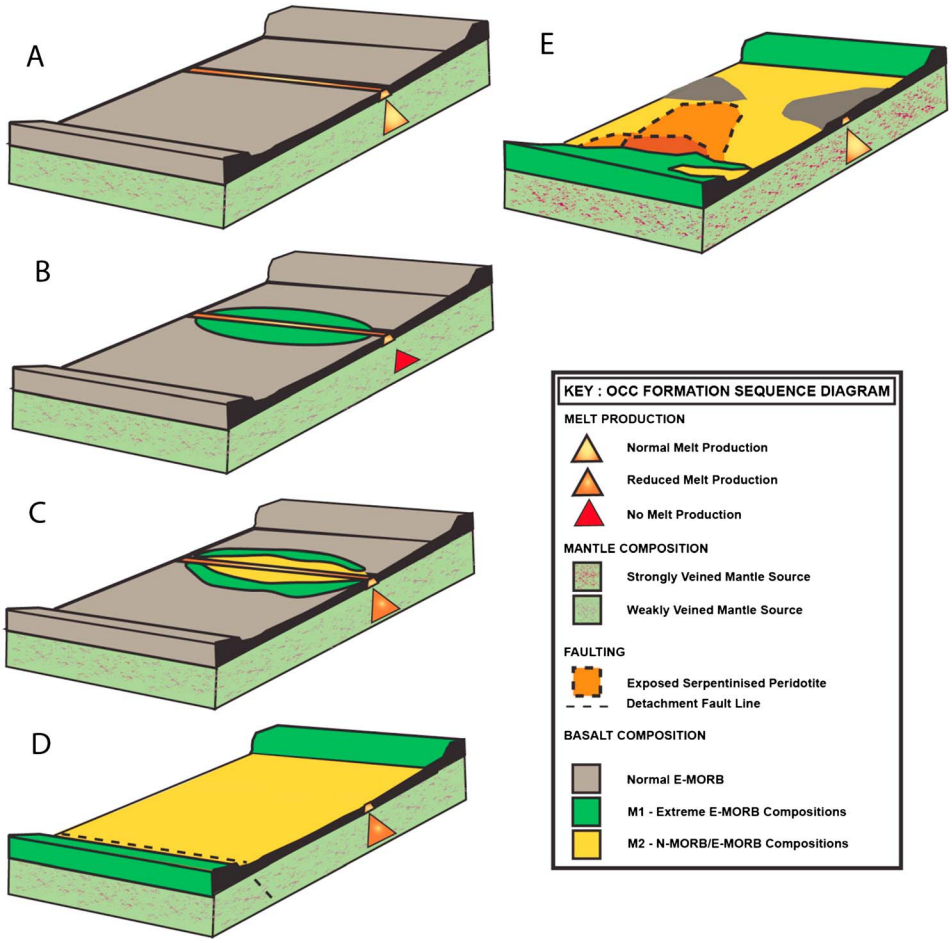

Figure 12. Sequential block diagram illustrating OCC development and its relation to underlying mantle composition. Block diagrams are shown for each developmental stage A-E.

Table 4. Average Crustal Thickness Estimates for Mid-Ocean Ridges and for Selected MAR Segments

Ridge/Region	Thickness (km)	Reference
Average 'Slow' Ridge	6.3	*White et al.* [1992, 2001]
Average 'Ultraslow' Ridge	4	
Average 'hotspot' Ridge	10	
MAR 5°S Northern Segment (segment end)	3	*Planert et al.* [2009]
MAR 5°S Northern Segment (segment Center)	8.5	
MAR 5°S Southern Segment (OCC)	2.5–5.0	
MAR 33–40°N (Segment Center)	8–9	*Detrick et al.* [1995]
MAR 33–40°N (Segment End)	<3–4	
13°19′N OCC, MAR (Segment Center)	~3.5 km	*MacLeod et al.* [2009]

production. Instead, at 13°19′N, source geochemistry (ultra-depleted harzburgitic mantle or UDMM) combined with melting of a few, low-solidus HIMU-FOZO veins, causes local cooling of the mantle further suppressing melt fraction, further promoting OCC formation.

Acknowledgments

[35] The authors would like to acknowledge NERC funding, and to thank Henry Dick for his thorough and insightful review.

References

Arevalo, R., and W. F. McDonough (2009), Chemical variations and regional diversity observed in MORB, *Chem. Geol.*, *271* (1–2), 70–85, doi:10.1016/j.chemgeo.2009.12.013

Armienti, P., and D. Gasperini (2007), Do we really need mantle components to define mantle composition? *J. Petrol.*, *48*(4), 693–709, doi:10.1093/petrology/egl078.

Blackman, D. K., et al. (2002), Geology of the Atlantis Massif (Mid-Atlantic Ridge, 30° N): Implications for the evolution of an ultramafic oceanic core complex, *Mar. Geophys. Res.*, *23*(5–6).

Bonnati, E., D. Brunelli, P. Fabretti, M. Ligi, R. A. Portaro, and M. Seyler (2001), Steady-state creation of crust-free lithosphere at cold spots in mid-ocean ridges, *Geology*, *29*(11), 979–982.

Buck, W. R., L. L. Lavier, and A. N. B. Poliakov (2005) Modes of faulting at mid-ocean ridges, *Nature*, *434*, 719–723, doi:10.1038/nature03358.

Cann, J. R., D. K. Blackman, D. K. Smith, E. McAllister, B. Janssen, S. Mello, E. Avgerinos, A. R. Pascose, and J. Escartín (1997), Corrugated slip surfaces formed at ridge-transform intersections on the Mid-Atlantic Ridge, *Nature*, *38*, 329–332.

Cannon, J. R. (1984), *The One–Dimensional Heat Equation, Encyclopedia of Mathematics and Its Applications, 23*, *1st ed.*: Addison-Wesley Publishing Company/Cambridge University Press, Massachusetts, ISBN 9780521302432

Detrick, R. S., H. D. Needham, and V. Renard (1995), Gravity anomalies and crustal thickness variations along the Mid-Atlantic Ridge between 33°N and 40°N, *J. Geophys. Res.*, *100*(B3), 3767–3787, doi:10.1029/94JB02649.

Dick, H. J. B., W. B. Bryan, and G. Thompson (1981), Low-angle detachment faulting and steady-state emplacement of plutonic rocks at ridge-transform intersections, *Eos, Trans., AGU*, *62*, 406.

Dick, H. J. B., M. A. Tivey, and B. E. Tucholke (2008), Plutonic foundation of a slow-spreading ridge segment: Oceanic core complex at Kane Megamullion, 23°30′N, 45°20′W. *Geochem. Geophys. Geosyst.*, *9*, 44, doi:10.1029/2007GC001645.

Donnelly, K. E., S. L. Goldstein, C. H. Langmuir, and M. Spiegelman (2004), Origin of enriched ocean ridge basalts and implications for mantle dynamics, *Earth. Planet. Sci. Lett.*, *226*, 347–366, doi:10.1016/j.epsl.2004.07.019.

Dosso, L., H. Bougault, J. L. Joron (1993), Geochemical morphology of the north Mid-Atlantic Ridge, 10-degrees-24-degrees-N — Trace element-isotope complementarity, *Earth. Planet. Sci. Lett.*, *120*(3–4), 443–462.

Drouin, M., M. Godard, B. Ildefonse, O. Bruguier, and C. Garrido (2009), Geochemical and petrographic evidence for magmatic impregnation in the oceanic lithosphere at Atlantis Massif, Mid-Atlantic Ridge (IODP Hole U1309D, 30°N), *Chem. Geol.*, *264*, 1–4, 30, 71–88, doi:http://dx.doi.org/10.1016/j.chemgeo.2009.02.013.

Escartín, J., C. Mével, C. J. MacLeod, and A. M. McCaig (2003), Constraints on deformation conditions and the origin of oceanic detachments: The Mid-Atlantic Ridge core complex at 15°45′N, *Geochem. Geophys. Geosyst.*, *4*(8), 1067, doi: 10.1029/2002GC000472

Escartín, J., D. K. Smith, J. Cann, H. Schouten, C. H. Langmuir, and S. Escrig (2008), Central role of detachment faults in accretion of slow-spreading oceanic lithosphere, *Nature*, *455*, 790–795, doi:10.1038/nature07333.

Godard, M., Y. Lagabrielle, O. Alard, and J. Harvey (2008), Geochemistry of the highly depleted peridotites drilled at ODP Sites 127 and 1274 (Fifteen-Twenty Fracture Zone, Mid-Atlantic Ridge): Implications for mantle dynamics beneath a slow spreading ridge, *Earth. Planet. Sci. Lett.*, *267*, 410–425, doi:10.1016/j.epsl.2007.11.058.

Hannigan, R. E., A. R. Basu, and F. Teichmann (2001), Mantle reservoir geochemistry from statistical analysis of ICP-MS trace element data of equatorial mid-Atlantic MORB glasses, *Chem. Geol.*, *175*, 397–428.

Hart S. R. (1984), A large-scale isotope anomaly in the southern hemisphere mantle, *Nature*, *309*, 753–757.

Hellebrand, E., Snow, J. E., Hoppe, P., and A. W. Hofmann (2002), Garnet-field melting and late-stage refertilisation in 'residual' abyssal peridotites from the Central Indian Ridge, *J. Petrol.*, *43*; 12.

Hémond, C., A. W. Hofmann, I. Vlastélic, and F. Nauret (2006), Origin of MORB enrichment and relative trace element compatibilities along the Mid-Atlantic Ridge between 10° and 24°N, *Geochem. Geophys. Geosyst.*, *7*(12), Q12010, doi:10.1029/2006GC001317

Hofmann, A. W. (1988), Chemical differentiation of the Earth: the relationship between mantle, continental crust, and oceanic crust, *Earth. Planet. Sci. Lett.*, *90*, 297–314.

Kelemen, P. B., E. Kikawa, D. J. Miller, and Shipboard Scientific Party (2004), Proceedings of the Ocean Drilling Program, Initial Reports, 209, Chapter 1, Leg 209 Summary, Ms 209SR-001

Lin, J., G. M. Purdy, H. Schouten, J.-C. Sempéré, and C. Zervas 1990, Evidence from gravity data for focused magmatic accretion along the Mid-Atlantic Ridge, *Nature*, *344*, 627–632, doi: 10.1038/344627a0.

Lissenberg C. J. and H. J. B. Dick (2008), Melt-rock reaction in the lower oceanic crust and its implications for the genesis of mid-ocean ridge basalt, *Earth and Planet Sci. Lett.*, *271*(1–4), 311–325, doi:http://dx.doi.org/10.1016/j.epsl.2008.04.023.

MacLeod, C. J., R. C. Searle, B. J. Murton, J. F. Casey, C. Mallows, S. C. Unsworth, K. L. Achenbach and M. Harris (2009), Life cycle of oceanic core complexes, *Earth. Planet. Sci. Lett.*, *287*, 333–344, doi:http://dx.doi.org/10.1016/j.epsl.2009.08.016.

McKenzie, D., and R. K. O'Nions (1991), Partial melt distributions from inversion of rare earth element concentrations, *J. Petrol.*, *32*(5), 1021–1091

Ohara, Y., T. Yoshida, Y. Kato, and S. Kasuga (2001), Giant megamullion in the Parece Vela Backarc Basin, *Mar. Geophys. Res*, *22*(1), 47–61.

Pertsev, A. N., N. S. Bortnikov, L. Ya Aranovich, E. A. Vlasov, V. E. Beltenev, V. N. Ivanov, and S. G. Simakin (2009), Peridotite–melt interaction under transitional conditions between the spinel and plagioclase facies beneath the Mid-Atlantic Ridge: Insight from peridotites at 13°N, *Petrology*, *17*(2), 124–137, doi:10.1134/S0869591109020027.

Planert, L., E. R. Flueh, and T. J. Reston (2009), Along- and across-axis variations in crustal thickness and structure at the Mid-Atlantic Ridge at 5°S obtained from wide-angle seismic tomography: Implications for ridge segmentation, *J. Geophys. Res.*, *114*(B9), B09102.1–B09102.20

Shaw, D. M. (1970), Trace element fractionation during anatexis, *Geochim. Cosmochim. Acta*, *34*, 237–243.

Seyler, M., J. P. Lorand, H. G. B. Dick, and M. Drouin (2007), Pervasive melt percolation reactions in ultra-depleted refractory harzburgites at the Mid-Atlantic Ridge, 15°20'N: ODP Hole 1274A, *Contrib. Mineral. Petrol.*, *153*, 303–319, doi:10.1007/s00410-006-0148-6.

Smith, D. K., J. R. Cann, and J. Escartín (2006), Widespread active detachment faulting and core complex formation near 138 N on the Mid-Atlantic Ridge, *Nature*, *442*, 440–443, doi:10.1038/nature4950.

Smith, D. K., J. Escartín, H. Schouten and J. R. Cann (2008), Fault rotation and core complex formation: Significant processes in seafloor formation at slow-spreading mid-ocean ridges (Mid-Atlantic Ridge, 13°–15°N), *Geochem. Geophys. Geosyst.*, *9*(3), Q03003, doi:10.1029/2007GC001699.

Suhr, G., H. A. Seck, N. Shimizu, D. Günther, G. Jenner (1998), Infiltration of refractory melts into the lowermost oceanic crust: evidence from dunite- and gabbro-hosted clinopyroxenes in the Bay of Islands Ophiolite, *Contrib. Mineral. Petrol.*, *131*(2–3), 136–154.

Suhr, G., E. Hellebrand, K. Johnson and D. Brunelli (2008), Stacked gabbro units and intervening mantle: A detailed look at a section of IODP Leg 305, Hole U1309D, *Geothem. Geophys. Geosyst.*, *9*, Q10007, 31, doi:10.1029/2008GC002012.

Sun, S. S., and W. F. McDonough (1989), Chemical and isotopic systematics of oceanic basalts: implications for mantle composition and processes, in Magmatism in the Ocean Basins, edited by A. D. Saunders, and M. J. Norry, J. Geol. Soc. Special Publications, 42, 313–345, The Geological Society Publishing House, Bath.

Tucholke, B. E., J. Lin and M. C. Kleinrock (1998), Megamullions and mullion structure defining oceanic metamorphic core complexes on the mid-Atlantic ridge, *J. Geophys. Res.*, *103*(B5), 9857–9866.

Tucholke, B. E., M. D. Behn, W. R. Buck, and J. Lin (2008), Role of melt supply in oceanic detachment faulting and formation of megamullions, *Geology*, *36*, 455–458, doi:10.1130/G24639A.1.

White, R. S., D. McKenzie, and R. K. O'Nions (1992), Oceanic crustal thickness from seismic measurements and rare earth element inversions, *J. Geophys. Res.*, *97*(19), 683–19,715

White, R. S., T. A. Minshull, M. J. Bickle, and C. J. Robinson (2001), Melt generation at very slow-spreading oceanic ridges: Constraints from geochemical and geophysical data, *J. Petrol.*, *42*, 1171–1196.

Workman, R. K. and S. R. Hart (2004), Major and trace element composition of the depleted MORB mantle (DMM), *Earth. Planet. Sci. Lett.*, *231*, 53–72, doi:http://dx.doi.org/10.1016%2fj.epsl.2004.12.005.

Yoder, H. S., and C. E. Tilley (1962), Origin of Basalt Magmas: An Experimental Study of Natural and Synthetic Rock Systems, *J. Petrol.*, *3*(3), 342–532, doi: 10.1093/petrology/3.3.342.